An artificial dielectric slab for ultra high-field MRI: proof of concept

Vorobyev, V.; Shchelokova, A.; Zivkovic, I.; Slobozhanyuk, A.; Baena, J.D.; Risco, J.P. del; ... ; Glybovski, S.

Note: To cite this publication please use the final published version (if applicable).

Communication

An artificial dielectric slab for ultra high-field MRI: Proof of concept

Vsevolod Vorobyev [a], Alena Shchelokova [a], Irena Zivkovic [b], Alexey Slobozhanyuk [a],
Juan D. Baena [c], Juan P. del Risco [d], Redha Abdeddaim [e], Andrew Webb [b], Stanislav Glybovski [a],*

[a] *Department of Physics and Engineering, ITMO University, 197101 St. Petersburg, Russia*
[b] *Department of Radiology, C.J. Gorter Center for High Field MRI, Leiden University Medical Center, Leiden 2333 ZA, the Netherlands*
[c] *Department of Physics, Universidad Nacional de Colombia, Bogota 111321, Colombia*
[d] *School of Exact Sciences and Engineering, Universidad Sergio Arboleda, Bogota 111711, Colombia*
[e] *Aix Marseille University, CNRS, Centrale Marseille, Institut Fresnel, F-13013 Marseille, France*

ARTICLE INFO

ABSTRACT

High-permittivity dielectric pads, i.e., thin, flexible slabs, usually consisting of mixed ceramic powders and liquids, have been previously shown to increase the magnetic field at high and ultra high-fields in regions of low efficiency of transmit coils, thus improving the homogeneity of images. However, their material parameters can change with time, and some materials they contain are bio incompatible. This article presents an alternative approach replacing ceramic mixtures with a low-cost and stable artificial dielectric slab. The latter comprises a stack of capacitive grids realized using multiple printed-circuit boards. Results in this article show that the proposed artificial dielectric structure can obtain the same increase in the local transmit radiofrequency magnetic field distribution in a head phantom at 7 T as the conventional dielectric pad.

1. Introduction

The number of ultra high-field magnetic resonance imaging (MRI) systems used for research applications has increased significantly over the past decade. Recently ultra high-field systems have been approved for clinical applications, although by using a single transmit radiofrequency (RF) channel [1]. Major driving forces are the increased signal-to-noise, susceptibility-weighted image contrast, angiographic capabilities, and spectroscopic resolution.

In terms of required hardware, the birdcage coil is the most common RF transmit device used in high-field clinical MRI. The coil is composed of a number (usually 16–32) of straight coupled conductors placed on a cylindrical surface and directed along the static magnetic field B_0 [2]. Two degenerate fundamental modes are excited in quadrature with sinusoidal/cosinusoidal distributions of currents in the rungs around the periphery of the coil. The corresponding circularly-polarized magnetic field B_1^+ created within

the coil in the low-frequency approximation (i.e., when the sample has minimal effect on RF propagation), has a homogeneous distribution. However, as the RF wavelength in the sample becomes comparable with the sample dimensions, the birdcage coil's transmit field becomes distorted. In essence, regions of increased and decreased transmit efficiency at sample-specific locations occur, making the spatial distribution of the flip angle of protons inhomogeneous. As a result, dark voids on MR images appear. One of the notable examples is neuroimaging at 7 T, where the RF magnetic field is transmitted at 298 MHz [3].

One of the methods to tailor the transmit field at the ultra high-field is to use RF-shimming with arrays of RF-coils, individually driven with specific phases and/or magnitudes [4–6]. While this parallel transmission (pTx) approach has become useful for biomedical research, its application in clinics is limited by the hardware complexity and difficulties in ensuring the RF safety of a patient during RF transmission with different shimming scenarios. As an alternative to pTx, passive RF shimming methods have been proposed, which up to now remain the only clinically acceptable way to homogenize flip-angle distribution in the region of interest. One of these methods is passive shimming with non-resonant surface RF coils, appropriately coupled to a volume transmit coil [7]. In the study in Ref. [7], the achieved improvement of

* Corresponding author.
E-mail addresses: vsevolod.vorobyev@metalab.ifmo.ru (V. Vorobyev), a.shchelokova@metalab.ifmo.ru (A. Shchelokova), I.Zivkovic@lumc.nl (I. Zivkovic), a.slobozhanyuk@metalab.ifmo.ru (A. Slobozhanyuk), jdbaenad@unal.edu.co (J.D. Baena), jpdelriscog@unal.edu.co (J.P. del Risco), redha.abdeddaim@fresnel.fr (R. Abdeddaim), A.Webb@lumc.nl (A. Webb), s.glybovski@metalab.ifmo.ru (S. Glybovski).

the B_1^+ was by factor 1/3 for 7 T brain imaging, when an inner-layer surface coil element was appropriately tuned above the Larmor frequency. Another widely known approach is based on the application of high-permittivity dielectric pads. Dielectric pads placed inside the standard birdcage transmit coil have been designed to improve the transmit field distribution, most commonly to increase the homogeneity. Many examples have been shown in the literature for human brain MRI at 7 T [8–10]. The displacement currents induced in the dielectric pads create a secondary magnetic field, which ideally adds constructively to the primary transmit field (directly created by the coil) in areas of low primary transmit efficiency. As a result, the overall RF magnetic field level in the whole region of interest is equalized [8]. The thinner the pad, the higher its relative permittivity is required to be to increase the local transmit RF magnetic field [9]. However, dielectric pads, usually based on mixtures of liquids and ceramic powders, have some drawbacks. Their material parameters can change with time, and some materials they may contain are bioincompatible [10]. Other previously reported methods to locally redistribute the field of a birdcage in the human head consist in using resonant metal-dielectric metasurfaces [11] and metal inclusions based on the Kerker effect [12].

To avoid some of the disadvantages of conventional pads, but achieve the same effect of the transmit field, in this work we propose a reliable device that is based on an artificial dielectric instead of conventional ceramic-containing mixtures. Artificial dielectrics are typically periodic structures made of metal or dielectric elements that support the propagation of slow waves with similar phase velocities in the operational band as in natural dielectric materials. Such structures have various realizations [13] and have been applied for more than seven decades in various antennas and microwave devices such as lenses, delay lines, and resonators [14,15]. For MRI we selected a realization that is non-resonant, stable in time, low-cost, and easy to manufacture.

2. Design and simulation of the artificial dielectric slab

To design an artificial dielectric slab for a birdcage coil for brain MRI at 7 T, we used stacked single-layer printed circuit boards (PCBs) with etched periodic structures of small square metal patches. Previous authors have shown that this geometry is equivalent over a broad range of frequencies to a uniaxial dielectric with high permittivity tensor components in the plane of the PCBs [16–18]. In other words, for a plane wave with normal incidence and polarization along the plane of patches, the structure behaves sim-

ilarly to a high-permittivity homogeneous dielectric. The unit cell of the artificial dielectric, shown in Fig. 1(a), consists of 4 layers: 2 layers of metal patches and 2 insulating layers. The patch layers are shifted relative to each other by half the period of the structure a, which is much smaller than the operational wavelength at the Larmor frequency of 300 MHz. Due to the lateral shift, each metal patch is capacitively coupled with eight surrounding patches [16]. The distance between the metallic layers h_d is much smaller than the period, which means that the broadside capacitance between patches in neighboring layers is much larger than the capacitance between the edges of adjacent patches within the same layer [16]. The dimensions of the artificial dielectric slab were chosen to produce a structure with the same effective permittivity as for conventional dielectric pads previously used for brain imaging [9]. The selected artificial dielectric was modeled analytically by the homogenization approach. For this structure, two approximate formulas are known to calculate the effective relative permittivity ε_{eff} concerning the electric field component parallel to the plane of the patches [16,18]. Here we used one of these formulas [16]: $\varepsilon_{eff} = [(a/2 - g)/h_d]^2$ to predict the geometric parameters of the unit cells in the first approximation.

To precisely predict the parameters required to achieve a given effective permittivity, a commercial electromagnetic software package (CST Microwave Studio), was used to calculate the reflection (R) and transmission (T) coefficients of a normally incident plane wave for the artificial dielectric layer. The layer was considered as infinite in the plane of the structure and had a thickness of 0.8 cm (10 stacked 0.079-cm thick PCBs). Based on the modeled reflection and transmission coefficients, the effective material parameters of the artificial dielectric were extracted using the Nicolson-Ross-Weir method [19,20]. The numerically calculated dependence of ε_{eff} on the geometry is shown in Fig. 1(b). We designed the real part of ε_{eff} to be approximately 120 since this value has been found previously to be optimal for 7 T human brain MRI for a conventional dielectric pad with a thickness of 0.8 cm. These properties were shown to provide a sufficient secondary magnetic field of induced displacement currents in the pad, that improve homogeneity in a human brain region. Such a relative dielectric permittivity is achieved in conventional pads using calcium titanate ($CaTiO_3$) suspension mixtures [9]. Also, we considered the manufacturing limitations of low-cost PCBs, which require $g \geqslant 0.03$ cm. The resulting geometrical parameters are $a = 0.9$ cm, $g = 0.06$ cm, $h_m = 0.0035$ cm, $h_d = 0.076$ cm, for a relative permittivity of the substrate $\varepsilon_{substrate} = 3.5$ and its loss tangent $\tan \delta = 0.0013$, which correspond to the material Arlon
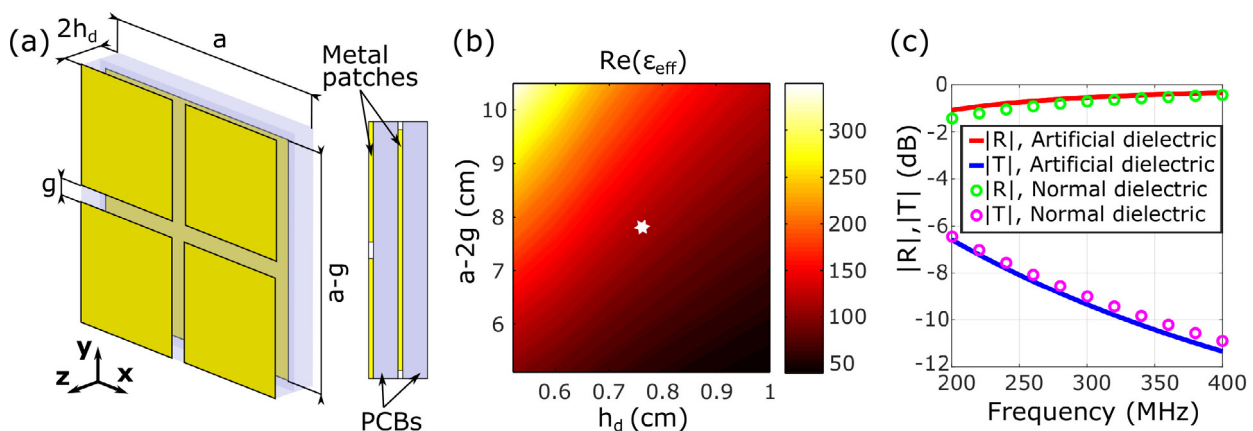

Fig. 1. Artificial dielectric model and its properties: (a) unit cell geometry (perspective and side views); (b) numerically calculated real part of the effective permittivity as a function of geometry; (c) simulated reflection and transmission coefficients vs. frequency for the infinite artificial dielectric slab $\varepsilon_{eff} = 120$ and dielectric slab with $\varepsilon_d = 120$ (normal incidence, thickness 0.8 cm).

25 N. As can be seen in Fig. 1(c), with the parameters mentioned above, the structure indeed demonstrates the same reflection and transmission coefficients for a normally-incident plane wave as those of the dielectric slab with relative permittivity of 120, the same thickness 0.8 cm and with loss tangent of 0.05.

The above results demonstrate that for a normally incident plane wave at 300 MHz, both the artificial dielectric slab and conventional dielectric pad have the same effect on the field distribution around them. However, their equivalence when excited by the transmit field of a birdcage coil still should be investigated. With this aim, the CST Time Domain solver was used to simulate the B_1^+ field distribution in a 7 T birdcage coil containing a head-mimicking phantom [21]. The coil parameters correspond to a commercially available birdcage head coil (Nova Medical), also considered in [8]. The coil had the following parameters: inner diameter $D_{inside} = 29$ cm, shield diameter $D_{shield} = 33$ cm, coil length $l_{coil} = 18$ cm. In numerical simulations, we considered three cases illustrated in Fig. 2(a-c). First, a reference case is presented in Fig. 2(a) describing the birdcage coil with the phantom. The phantom with a relative permittivity of 50 and a conductivity of 0.6 S/m with approximate dimensions $27 \times 22 \times 18$ cm^3 was used in both numerical and experimental studies. In the second case, a dielectric pad with dimensions $11.3 \times 7.7 \times 0.8$ cm^3 was placed directly adjacent to the phantom, as shown in Fig. 2(b). The sizes of the dielectric pad were chosen to fit with the available space inside the RF coil. Conventional pad material parameters used in simulation are $Re(\varepsilon_{pad}) = 120$ and $\tan \delta_{pad} = 0.05$. The third case is the artificial dielectric slab in place of the conventional pad [see Fig. 2(c)]. A schematic view of the artificial dielectric slab having the same dimensions $11.3 \times 7.7 \times 0.8$ cm^3 is presented in supple-

mentary Fig. 1. Both conventional dielectric pad and artificial dielectric slab were placed as close as possible to the phantom. It is worth noting that an increase in distance between the sample and the conventional dielectric pad would lead to the reducing of the effect [10]. The same effect can be seen for the artificial dielectric slab.

The simulated B_1^+-field and electric field distributions in the *XZ* (coronal) plane through the center of the phantom for the cases in Fig. 2(a-c) are presented in Fig. 2(e-j), respectively. In the dielectric pad case [Fig. 2(f)], we observe a 1.15-fold increase in the B_1^+-field amplitude in comparison with the reference case [Fig. 2(e)] at the distance of 2 cm from the top of the phantom marked by the black arrow. In both cases [Fig. 2(e) and Fig. 2(g)] we observed 1.15-fold increase in the B_1^+-field amplitude in marked area. Fig. 2(d) gives a more detailed look on B_1^+ field profiles taken from the maps along the dashed black lines. At the same location as above [shown by black circle in Fig. 2(i,j)] the enhancements of the $|E|$-field for the dielectric pad and artificial dielectric slab cases were 1.08 and 1.04 correspondingly. Thus, the results show that the artificial finite-sized dielectric slab exhibits the same local electromagnetic field modification in the phantom as the conventional pad both for a normally incident plane wave and for excitation by the birdcage coil.

In order to check how the presence of the artificial dielectric slab affects the specific absorption rate (SAR), we performed electromagnetic simulations of the virtual voxel human model "Duke" [22] cropped at the level of the shoulders with a 0.2-cm resolution. The B_1^+-field and SAR (averaged over 10 g of tissue) maps were calculated using CST Time Domain solver and the same model of the birdcage head coil. The results are presented in Fig. 3. The same
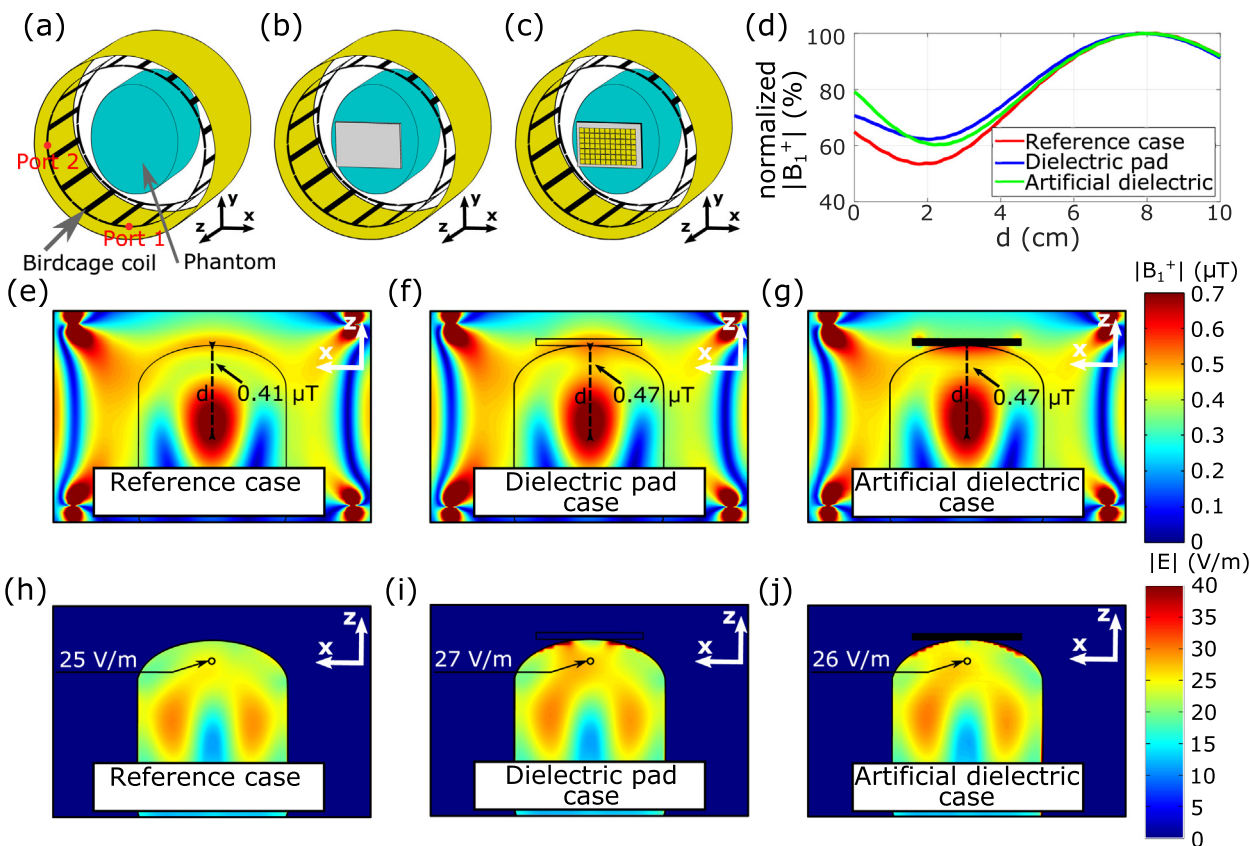

Fig. 2. Simulation of three cases: (a) an elliptical homogeneous phantom inside a shielded birdcage head coil; (b) the same with a high-permittivity pad attached to the phantom; (c) the same with the proposed artificial dielectric slab instead of conventional pad. (d) B_1^+ field profiles for the same three cases. (e,f,g) B_1^+-field distribution in the *XZ*-plane corresponding to 1 W of accepted transmit power; (h,i,j) $|E|$-field distribution in the *XZ*-plane normalized to the same accepted power for each case.

local transmit RF magnetic field enhancement as for the phantom study was obtained for the cases with conventional dielectric pad and artificial dielectric slab (see B_1^+-field profiles in supplementary Fig. 2). For the reference case and ones with the high-permittivity pad and artificial dielectric slab, the maximum SAR, calculated for 1 W accepted power, values are 0.558 W/kg, 0.565 W/kg, and 0.57 W/kg, respectively. The hot spot location is in the eye area for all three cases.

3. Experiment

To confirm the numerically predicted equivalence between the dielectric pad and artificial dielectric slab, we experimentally measured transmit field maps inside a head-mimicking phantom [21]. Experimental results were obtained on Philips Achieva 7 T whole-body MRI scanner. B_1^+ maps were acquired using a DREAM sequence with acquisition parameters: TE = 1.975 ms, TR = 15 ms, flip angle=10°, STEAM angle=50°, voxel size $0.5 \times 0.5 \times 0.5$ cm^3. The artificial dielectric slab had the same parameters as the structure, which was simulated. It was constructed of a stack of five PCBs with double-sided metallization, into which the two-dimensional periodic system of patches was engraved by milling. The boards were made on 0.076-cm-thick

Arlon 25 N substrates and the metallization had the following parameters: $a = 0.9$ cm, $g = 0.06$ cm, $h_m = 0.0035$ cm. The size of the entire metallization of the artificial dielectric slab in the XY-plane was 11.3×7.7 cm^2. The conventional dielectric pad used for comparison was based on CaTiO$_3$ ceramic powder mixed with heavy water. It had the same geometric dimensions and the same material proprieties as in the simulations. The phantom parameters correspond to the ones used in simulation as well. The artificial dielectric slab, dielectric pad, and phantom used in the experiment are shown in Fig. 4(a). The measured transmit field increase [Fig. 4 (c,d,e)] confirms the simulation results from Fig. 2(e,f,g). Namely, both the artificial dielectric slab and conventional dielectric pad have been confirmed to provide the same increase of the transmit field distribution of the birdcage over the region of the local minimum. The precise values for these increases as a one-dimensional profiles are presented in Fig. 4(b).

4. Discussion and conclusions

Electromagnetic simulations and experimental data have shown that artificial dielectrics can enhance the local transmit magnetic field inside a phantom in an area corresponding to the parietal lobes of a human brain at 7 T. The improvement in B_1^+ field
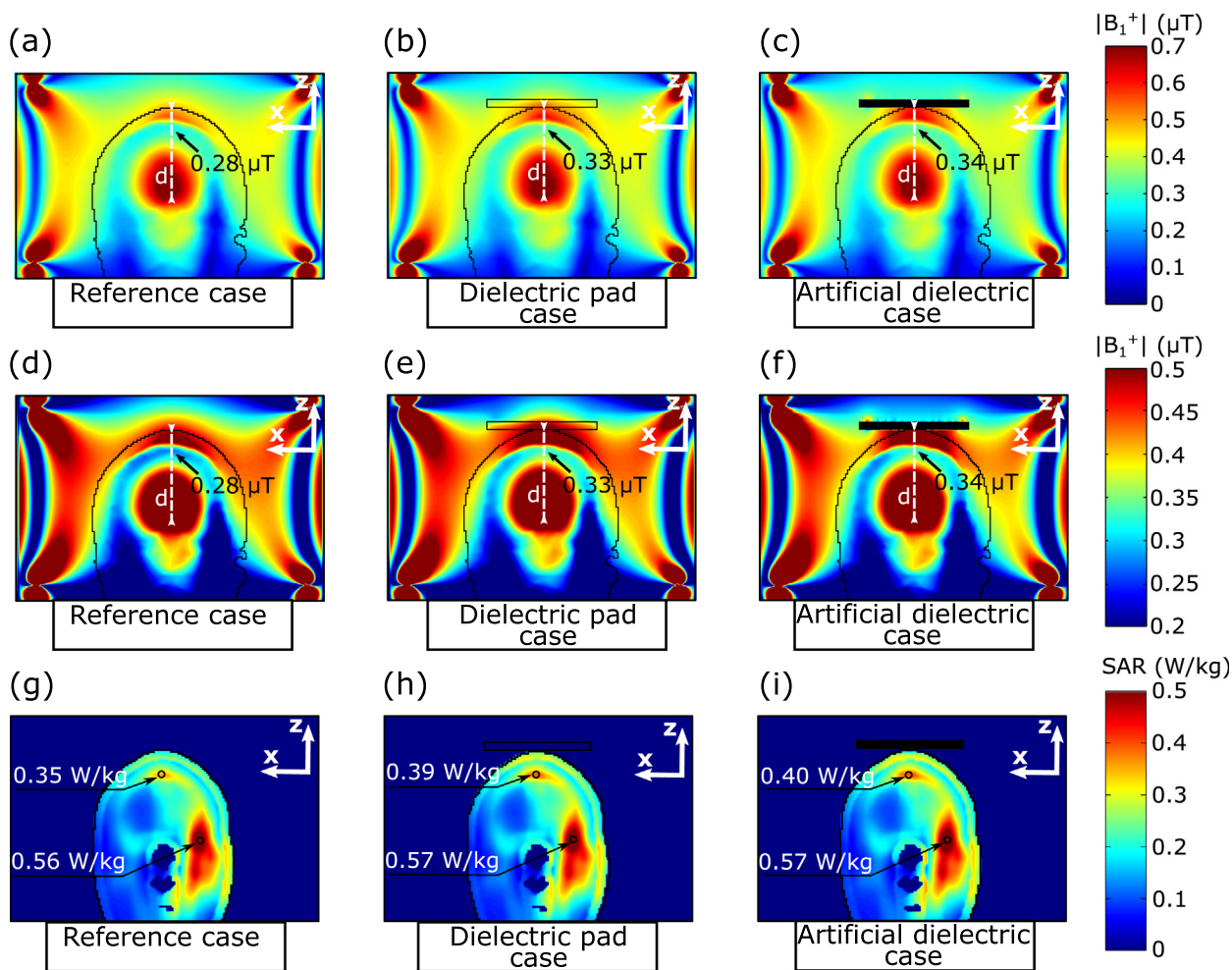

Fig. 3. Numerical simulation results of the B_1^+-field and SAR (averaged over 10 g of tissue) for 1 W of accepted transmit power for three cases: (a,d,g) human voxel model cropped at the level of the shoulders inside a shielded birdcage head coil; (b,e,h) the same with a high-permittivity dielectric pad attached closely to the head; (c,f,i) the same with the proposed artificial dielectric slab instead of a conventional pad. The B_1^+-field maps are shown for the central plane ($Y = 0$ cm) across the head, while SAR maps are build up through the local maximum plane ($Y = 2.4$ cm). The B_1^+-field maps (a,b,c) present the full scale images of the field for all 3 cases, while (d,e,f) are intended to better showcase the field difference in an area marked by black arrow between three cases.
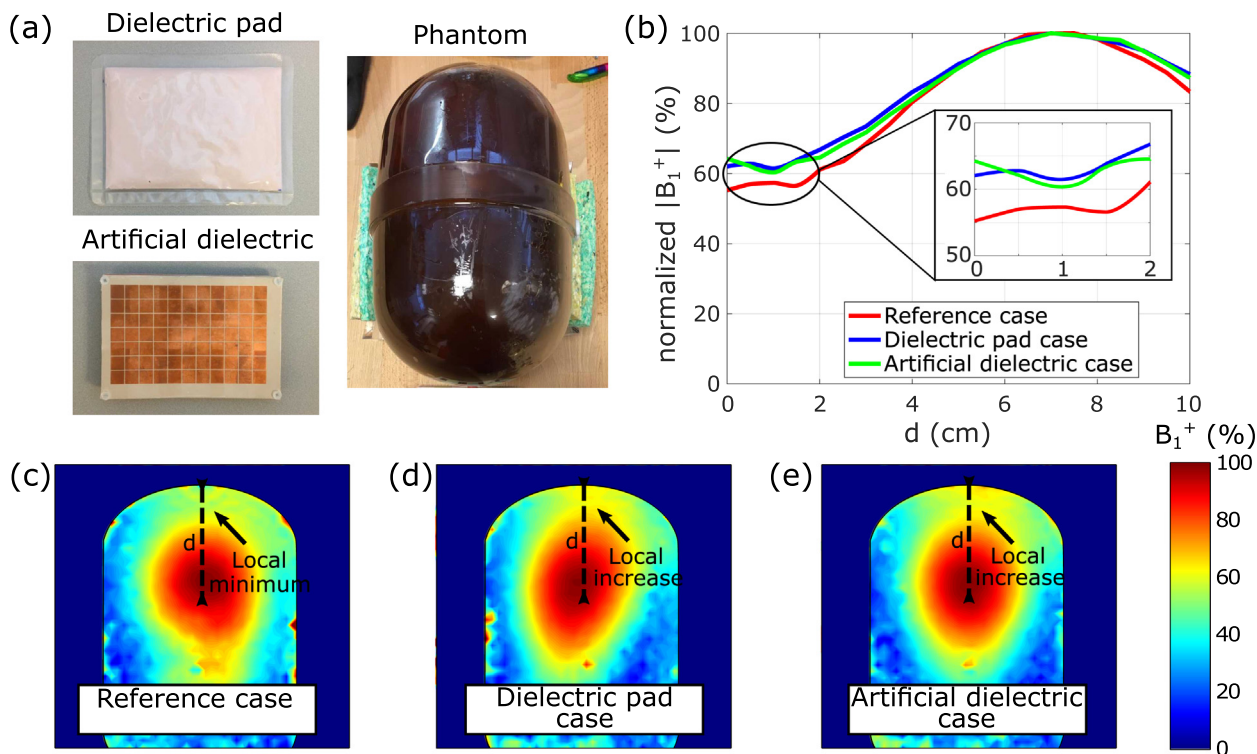
Fig. 4. (a) Photographs of the dielectric pad, artificial dielectric slab, and phantom used in the experiment. (b-e) B_1^+ field profiles and maps for three experimental cases: (c) reference case (no pads or structures used), (d) dielectric pad, (e) artificial dielectric slab. B_1^+ field magnitude was plotted at a depths d measured from the top surface of the phantom in the z-direction.

is more than 10%, which is very similar to the one of a conventional dielectric pad with the same dimensions. Importantly, once optimized for a plane-wave excitation by simulations, the proposed artificial pad remains equivalent to a conventional ceramic pad even inside a transmit birdcage coil.

Since conventional dielectric pads are typically lossy, the PCBs used for the artificial dielectric slab can also be lossy without reduced performance compared to the conventional pad. It has been checked that values of dielectric loss tangent up to 0.05, which are typical for Arlon, Rogers, or even cheap FR4 commercially available substrate materials, do not affect the performance of the artificial dielectric. Thus, the proposed artificial dielectric slab can be low-cost, unlike the conventional pad based on relatively expensive ceramics. As a result, increased availability and reduced cost are among the advantages of the proposed approach. The limitation of the proposed artificial dielectric slab is its stiffness in comparison with a conventional pad, which bends around the investigated sample better. Although a single 0.079-cm-thick layer of the artificial dielectric slab is flexible enough, the chosen geometry by its design requires ten stacked PCBs to achieve the same slab thickness as for the dielectric pad, ensuring the same electromagnetic properties. Designing of the artificial dielectric slab geometry in order to create a thinner, flexible structure is the task for future work. An increase in artificial pad dimensions leads to the enhancement of the local transmit magnetic field amplitude and to the expansion of the covered area, and the same applies to the conventional pad [23]. However, still, it is essential to optimize the dimensions and properties of both structures according to the area of interest.

Although the proposed artificial dielectric slab is anisotropic, once positioned as in Fig. 2(c), it is excited by the birdcage field similarly to a normally incident plane wave. Indeed, there is an electric field component in the plane of the structure tangent to

the patches. Moreover, close to the axis of the coil, the field can be represented by a sum of plane waves traveling in the positive and negative directions of z-axis. Note that in most scenarios of brain imaging, the dielectric pad is placed in a different way: parallel to the axis of the birdcage coil (nearby temporal lobes). However, the excitation produced by the birdcage coil is improper for the artificial dielectric slab in this desirable orientation. Indeed, far off the axis of the birdcage, the effective direction of local plane-wave propagation turns into parallel to the artificial dielectric slab. In this case, the structure does not increase the RF field anymore. Further research is needed to adapt the artificial dielectric slab to the proper position by using other metallization structures such as so-called fishnet metamaterials [24]. Nevertheless, the proposed artificial dielectric slab constructed of PCB patches can be considered a low-cost and time-stable alternative to ceramic pads for passive RF shimming, e.g., in 7 T imaging of parietal lobes.

Declaration of Competing Interest

None.

Appendix A. Supplementary material

Supplementary data associated with this article can be found, in the online version, at https://doi.org/10.1016/j.jmr.2020.106835.

References

[1] FDA, Fda clears first 7t magnetic resonance imaging device, https://www.fda.gov/news-events/press-announcements/fda-clears-first-7t-magnetic-resonance-imaging-device, Last accessed on 2020-07-25 (2017).

[2] C.E. Hayes, W.A. Edelstein, J.F. Schenck, O.M. Mueller, M. Eash, An efficient, highly homogeneous radiofrequency coil for whole-body NMR imaging at 1.5 T, J. Magn. Reson. (1969) 63 (3) (1985) 622–628.

[3] A.G. Webb, C.M. Collins, Parallel transmit and receive technology in high-field magnetic resonance neuroimaging, Int. J. Imaging Syst. Technol. 20 (1) (2010) 2–13.

[4] W. Grissom, C.-Y. Yip, Z. Zhang, V.A. Stenger, J.A. Fessler, D.C. Noll, Spatial domain method for the design of rf pulses in multicoil parallel excitation, Magn. Reson. Med. 56 (3) (2006) 620–629.

[5] W.A. Grissom, L. Sacolick, M.W. Vogel, Improving high-field MRI using parallel excitation, Imag. Med. 2 (6) (2010) 675–693.

[6] A.J.E. Raaijmakers, O. Ipek, D.W.J. Klomp, C. Possanzini, P.R. Harvey, J.J.W. Lagendijk, C.A.T. van den Berg, Design of a radiative surface coil array element at 7 T: The single-side adapted dipole antenna, Magn. Reson. Med. 66 (5) (2011) 1488–1497.

[7] S. Wang, J. Murphy-Boesch, H. Merkle, A.P. Koretsky, J.H. Duyn, B1 homogenization in mri by multilayer coupled coils, IEEE Trans. Med Imag. 28 (4) (2009) 551–554.

[8] A. Webb, Dielectric materials in magnetic resonance, Concepts Magn. Reson. Part A 38A (4) (2011) 148–184.

[9] W.M. Teeuwisse, W.M. Brink, K.N. Haines, A.G. Webb, Simulations of high permittivity materials for 7 T neuroimaging and evaluation of a new barium titanate-based dielectric, Magn. Reson. Med. 67 (4) (2012) 912–918.

[10] A.L. Neves, L. Leroi, Z. Raolison, N. Cochinaire, T. Letertre, R. Abdeddaïm, S. Enoch, J. Wenger, J. Berthelot, A.-L. Adenot-Engelvin, N. Malléjac, F. Mauconduit, A. Vignaud, P. Sabouroux, Compressed perovskite aqueous mixtures near their phase transitions show very high permittivities: New prospects for high-field MRI dielectric shimming, Magn. Reson. Med. 79 (2018) 1753.

[11] R. Schmidt, A. Slobozhanyuk, P. Belov, A. Webb, Flexible and compact hybrid metasurfaces for enhanced ultra high field in vivo magnetic resonance imaging, Scient. Rep. 7 (1) (2017) 1678.

[12] M. Dubois, L. Leroi, Z. Raolison, R. Abdeddaim, T. Antonakakis, J. de Rosny, A. Vignaud, P. Sabouroux, E. Georget, B. Larrat, G. Tayeb, N. Bonod, A. Amadon, F. Mauconduit, C. Poupon, D. Le Bihan, S. Enoch, Kerker effect in ultrahigh-field magnetic resonance imaging, Phys. Rev. X 8 (2018) 031083.

[13] R.A. Silin, Optical properties of artificial dielectrics (review), Radiophys. Quant. Electron. 15 (6) (1972) 615–624.

[14] I. Awai, T. Kubo, T. Iribe, D. Wakamiya, A. Sanada, An artificial dielectric material of huge permittivity with novel anisotropy and its application to a microwave BPF, IEEE MTT-S Int. Microwave Symp. Digest 2003 (2) (2003) 1085–1088.

[15] K. Takahagi, E. Sano, High-gain silicon on-chip antenna with artificial dielectric layer, IEEE Trans. Antennas Propag. 59 (10) (2011) 3624–3629.

[16] J.P. del Risco, J.D. Baena, Extremely thin Fabry-Perot resonators based on high permittivity artificial dielectric, in: 2016 10th International Congress on Advanced Electromagnetic Materials in Microwaves and Optics (METAMATERIALS), 2016, pp. 40–42.

[17] S. Barzegar-Parizi, B. Rejaei, Calculation of effective parameters of high permittivity integrated artificial dielectrics, IET Microwaves, Antennas Propag. 9 (12) (2015) 1287–1296.

[18] T. Chang, J.U. Kim, S.K. Kang, H. Kim, D.K. Kim, Y.-H. Lee, J. Shin, Broadband giant-refractive-index material based on mesoscopic space-filling curves, Nat. Commun. 7 (1) (2016) 12661.

[19] O. Luukkonen, S. Maslovski, S. Tretyakov, A stepwise Nicolson-Ross-Weir - based material parameter extraction method, IEEE Antennas Wirel. Propag. Lett. 10 (2011) 1295–1298.

[20] A.M. Nicolson, G.F. Ross, Measurement of the intrinsic properties of materials by time-domain techniques, IEEE Trans. Instrum. Meas. 19 (4) (1970) 377–382.

[21] W.M. Brink, Z. Wu, A.G. Webb, A simple head-sized phantom for realistic static and radiofrequency characterization at high fields, Magn. Reson. Med. 80 (4) (2018) 1738–1745.

[22] A. Christ, W. Kainz, E. Hahn, K. Honegger, M. Zefferer, E. Neufeld, W. Rascher, R. Janka, W. Bautz, J. Chen, B. Kiefer, P. Schmitt, H. Hollenbach, J. Shen, M. Oberle, D. Szczerba, A. Kam, J. Guag, N. Kuster, The virtual family–development of surface-based anatomical models of two adults and two children for dosimetric simulations, Phys. Med. Biol. 55 (2) (2010) N23–38.

[23] J. van Gemert, W. Brink, A. Webb, R. Remis, High-permittivity pad design tool for 7 T neuroimaging and 3 T body imaging, Magn. Reson. Med. 81 (2019) 3370–3378.

[24] K. Rustomji, R. Abdeddaim, J. Achard, M. Chmiaa, E. Georget, M. Goniche, W. Helou, J. Hillairet, S. Enoch, G. Tayeb, Mimicking electromagnetic wave coupling in tokamak plasma with fishnet metamaterials, Scient. Rep. 8 (1) (2018) 5841.